A Compton-thick AGN in the barred spiral galaxy NGC 4785

P. Gandhi,[1,2]★ S. Yamada,[3] C. Ricci,[4] D. Asmus,[5] R. F. Mushotzky,[6] Y. Ueda,[4]
Y. Terashima[7] and V. La Parola[8]

[1]*School of Physics & Astronomy, University of Southampton, Highfield, Southampton SO17 1BJ, UK*
[2]*Department of Physics, Durham University, South Road, Durham DH1 3LE, UK*
[3]*Tokyo Metropolitan University, 1–1 Minami-Osawa, Hachioji-shi, Tokyo 192-0397, Japan*
[4]*Department of Astronomy, Kyoto University, Kitashirakawa-Oiwake-cho, Sakyo-ku, Kyoto 606-8502, Japan*
[5]*European Southern Observatory, Alonso de Cordova, Vitacura, Casilla 19001, Santiago, Chile*
[6]*Department of Astronomy, University of Maryland, College Park, MD 20742, USA*
[7]*Department of Physics, Ehime University, 2-5, Bunkyo-cho, Matsuyama, Ehime 790-8577, Japan*
[8]*INAF, Istituto di Astrofisica Spaziale e Fisica Cosmica, via U. Malfa 153, 90146 Palermo, Italy*

ABSTRACT

We present X-ray observations of the active galactic nucleus (AGN) in NGC 4785. The source
is a local Seyfert 2 which has not been studied so far in much detail. It was recently detected with
high significance in the 15–60 keV band in the 66-month *Swift*/BAT (Burst Array Telescope)
all sky survey, but there have been no prior pointed X-ray observations of this object. With
Suzaku, we clearly detect the source below 10 keV, and find it to have a flat continuum and
prominent neutral iron fluorescence line with equivalent width $\gtrsim$1 keV. Fitting the broad-band
spectra with physical reflection models shows the source to be a Compton-thick AGN with N_H
of at least 2×10^{24} cm^{-2} and absorption-corrected 2–10 keV X-ray power $L_{2-10} \sim$ few times
10^{42} erg s^{-1}. Realistic uncertainties on L_{2-10} computed from the joint confidence interval on
the intrinsic power-law continuum photon index and normalization are at least a factor of 10.
The local bona fide Compton-thick AGN population is highly heterogeneous in terms of *WISE*
mid-infrared source colours, and the nucleus of NGC 4785 appears especially sub-dominant
in the mid-infrared when comparing to other Compton-thick AGN. Such sources would not
be easily found using mid-infrared selection alone. The extent of host galaxy extinction to the
nucleus is not clear, though NGC 4785 shows a complex core with a double bar and inner disc,
adding to the list of known Compton-thick AGN in barred host galaxies.

Key words: X-rays: individual: NGC 4785 – X-rays: individual: NGC 4945.

1 INTRODUCTION

Accurate assessment of the number density of highly obscured
active galactic nucleus (AGN) remains a topic of intense inter-
est. Compton-thick AGN (with line-of-sight column densities of
$N_H \gtrsim 1.5 \times 10^{24}$ cm^{-2}) are expected to constitute a substantial
fraction of the entire AGN population (Matt et al. 2000; Comas-
tri et al. 1995; Fabian & Iwasawa 1999; Gandhi & Fabian 2003;
Gilli, Comastri & Hasinger 2007; Treister, Urry & Virani 2009;
Draper & Ballantyne 2010; Akylas et al. 2012; Ueda et al. 2014).
Yet, their census appears to be far from complete. This is because
photoelectric absorption and Compton scattering in the obscuring
material (generally attributed to the $\sim$ pc-scale circumnuclear torus
of AGN unification schemes) results in severe attenuation of the di-
rect AGN continuum below 10 keV, and higher energy observations
are needed for probing this component. At much higher columns,

the only components to remain visible may be the reflected and scat-
tered components, whose emitted flux is typically just a few per cent,
or less, of the intrinsic AGN power (Iwasawa, Fabian & Matt 1997;
Arévalo et al. 2014; Baloković et al. 2014; Gandhi et al. 2014). This
makes identification and characterization of Compton-thick AGN
(hereafter CTAGN) a daunting task.

Somewhat paradoxically, CTAGN at high redshift may be more
easily identified because of the redshifting of high-energy rest frame
X-rays to below 10 keV. The exquisite point spread function and
sensitivity of *Chandra* and deep follow up with *XMM–Newton* over
this energy range have resulted in the compilation of a few repre-
sentative samples of distant CTAGN (Georgantopoulos et al. 2013;
Brightman et al. 2014).

In the local universe, probing the intrinsic continuum of CTAGN
requires an ability to detect photons over the observed frame energy
range above 10 keV, where, until recently, sensitive instruments have
been lacking. As a result, only about 20 CTAGN are known that are
well characterized based upon multiple observations, including a
detection above 10 keV as well as a fluorescence iron Kα emission

★ E-mail: poshak.gandhi@durham.ac.uk

line at 6.4 keV characteristic of reflection (Della Ceca et al. 2008; Goulding et al. 2012; Gandhi et al. 2014). There is also a known degeneracy between the CTAGN fraction and the reflection fraction in AGN population studies based upon moderate quality X-ray spectra (e.g. Gandhi et al. 2007; Treister et al. 2009). Increasing the number of these 'bona fide' CTAGN is thus important for an accurate census of obscured accretion in the local universe.

Swift/BAT (Gehrels et al. 2004; Barthelmy et al. 2005) is carrying out the most sensitive survey of the high-energy sky, over a full observed energy range of 14–195 keV. There are two complementary and independent processings of the Burst Array Telescope (BAT) maps, one by the Goddard team (cf. Tueller et al. 2008, 2010; Baumgartner et al. 2013) and one by the Palermo team which uses modified energy bands (cf. Cusumano et al. 2010a,b; Segreto et al. 2010). These have slightly differing optimizations, but there is broad agreement between both. The latest catalogues reach 4.8 σ flux limits of $\sim 10^{-11}$ erg s^{-1} cm^{-2} over 50 per cent of the sky.[1]

Follow-up and cross-matching of this survey has provided new insights on AGN in hard X-rays. Results include a new hard X-ray luminosity function (Burlon et al. 2011), measuring the anticorrelation between luminosity and column densities in Compton-thin AGN (Winter et al. 2009; Vasudevan et al. 2013; Ricci et al. 2014), and insights into AGN triggering as a result of mergers (Koss et al. 2010). Cross-matching with all-sky infrared catalogues has provided new diagnostics for identification of various AGN classes (e.g. Ichikawa et al. 2012; Matsuta et al. 2012; Maselli et al. 2013). Finally, follow-up with low-energy X-ray missions, especially *Suzaku*, has proven to be very effective in identifying previously missed sources, including AGN with tori providing strong reflection and/or Compton-thick absorption (Ueda et al. 2007; Severgnini et al. 2011; Gandhi et al. 2013).

Here, we present new *Suzaku* follow-up observations of NGC 4785, selected as a little studied Seyfert (Sy) 2 galaxy first detected in hard X-rays on the 66-month BAT maps by the Palermo group. The host galaxy is classified as a barred spiral [(R')SB(r)b] according to the Third Reference Catalogue of Bright Galaxies (de Vaucouleurs et al. 1991). Despite having been recognized as a nearby ($z = 0.0123$) Sy 2 almost three decades ago (Fairall 1986), the AGN properties remain unknown to a large degree. For instance, there has been no pointed observation of the source with any X-ray mission to date. And though the [O III]/Hβ optical emission line flux ratio is known to be very high (Fairall 1986), no absolute emission line fluxes have been published, to our knowledge.[2]

Suzaku reveals the source to be reflection-dominated over $\sim$2–10 keV. The combination of *Suzaku* and *Swift*/BAT data is used to model the broad-band X-ray spectrum and show the source to be obscured by Compton-thick obscuration during the observation. We discuss the origin of the broad-band X-ray emission, constraints on the intrinsic source power, and implications for multiwavelength studies of the CTAGN population in general. Luminosities quoted herein are based upon a redshift $z = 0.013\,11$ corrected to the reference frame of the cosmic microwave background and with a flat Planck cosmology with $H_0 = 67.3$ km s^{-1} Mpc^{-1} and $\Omega_\Lambda = 0.685$ (Planck Collaboration XVI 2014), corresponding to a distance of 59 Mpc. Note that a Tully–Fisher-based distance of 49.6 Mpc is reported in the literature (Theureau et al. 2007), but other complementary redshift-independent measurements are lacking. So we use the redshift-based distance herein. All X-ray spectral fitting is carried out with the XSPEC package v12.8.1g (Arnaud 1996) and uncertainties are quoted at 90 per cent confidence, unless stated otherwise.

2 OBSERVATIONS

2.1 *Swift*

The BAT on board *Swift* is a coded mask detector with a field of view of 1.4 sr (half-coded) and a pseudo-random mask pattern which aids in avoiding ghost images. The detector plane is a large array of gap-separated CdZnTe elements. The point spread function has side lobes extending over the whole image, but with an on-axis full width half-maximum (FWHM) of 22 arcmin.

The raw data are accumulated in the form of detector plane histograms consisting of an energy spectrum for each detector pixel. The custom code BATIMAGER (Segreto et al. 2010) then processes these histograms to generate all the final products. Background-subtracted sky map reconstruction is carried out by cross-correlating the observed mask shadowgrams with a decoding array derived from the projection of the mask pattern on to the detector plane, balanced and renormalized appropriately to account for detector defects (Goldwurm et al. 2003). The individual detector pointings are mosaicked into a final accumulated sky image by projection on to a common sky reference system under the spherical projection of the HEALPIX system (Górski et al. 2005). The skymap noise include both Poisson and coding noise and source detection in the final mosaics is carried out by a blind localization to search for pixels with a significance in excess of a pre-defined threshold in terms of the local noise. Finally, the identified candidates are cross-correlated with known source catalogues at other wavelengths. Full details of the BAT analysis steps may be found in Segreto et al. (2010).

NGC 4785 was first presented as a detection above 10 keV in the 66-month BAT catalogue,[3] where the X-ray detection has a signal-to-noise ratio (S/N) of 7 in the most sensitive band of 15–60 keV. More recent processings in progress have improved the S/N to 9.1 in the 100 month catalogue.[4] The X-ray source is offset by 0.54 arcmin from the optical coordinates of NGC 4785, well within the BAT positional uncertainty.

Here, we use the most recent data from the Palermo team which is a cumulative exposure of $\approx$112 months. The full source spectrum was extracted in eight energy channels between 15 and 150 keV, by deriving the source count rate at the nominal pixel position from the all-sky maps built in the corresponding eight energy bands. The response matrix is publicly available with the BAT 66 month catalogue.
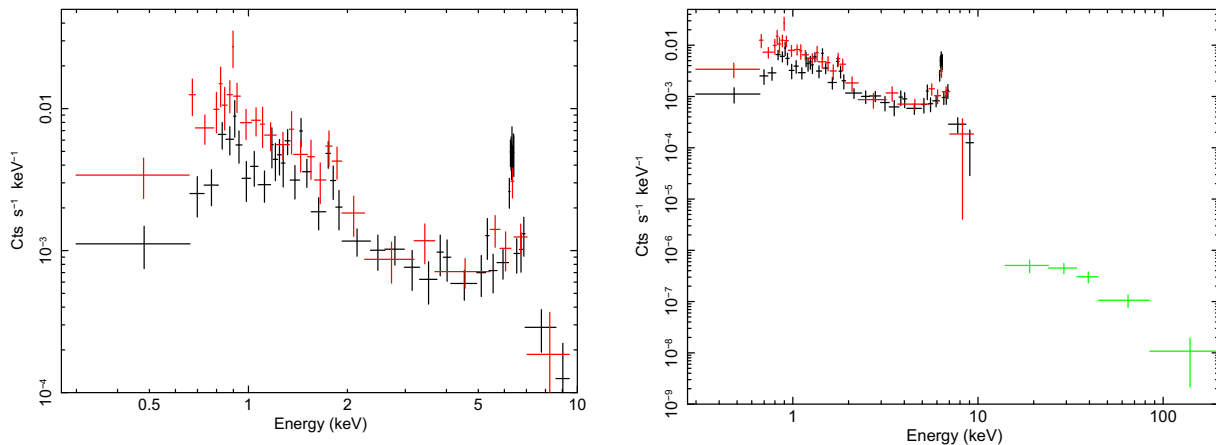
2.2 *Suzaku*

Suzaku observed NGC 4785 on 2013-07-22 (ObsID 708003010) for an exposure of 79 388 s. The low-energy instrument called the X-ray Imaging Spectrometer (XIS; Koyama et al. 2007) and the high-energy Hard X-ray Detector (HXD; Takahashi et al. 2007; Kokubun et al. 2007) were both operated in their standard modes with an XIS-nominal pointing.

---

[1] The base band for fluxes used by the Goddard group is 14–195 keV, while the Palermo group use 15–150 keV.

[2] Similarly, [N II] λ6584/Hα is also high in data presented by Márquez et al. (2004).

[3] http://bat.ifc.inaf.it/

[4] Ibid.

Figure 1. *Suzaku* spectra of NGC 4785 for the XIS on the left. The combined FI spectrum is in black and the BI spectrum in red. The right-hand panel additionally shows the *Swift*/BAT spectrum in green.

The standard *Suzaku* software available as part of FTOOLS v6.15.1 (Blackburn 1995) was used for data reduction. Cleaned event files were generated using standard filtering with pipeline v2.8.20.35 processing and used for the analysis herein. A 3.4-arcmin radius circular aperture was used for integrating XIS source counts, and background counts were extracted from external source-free regions using a polygonal region. The *Suzaku* calibration data base dated 2014-05-23 was used for generating response matrices (RMFs) and auxiliary response files (ARFs). The responses of the two front-illuminated (FI) CCDs XIS0 and XIS3 match closely, so the spectra and responses were combined into one. The spectrum from the back-illuminated (BI) detector XIS1 was treated separately. For fitting, the spectra were grouped to have a minimum S/N of at least 3 per energy bin after background subtraction.

For HXD/PIN (sensitive between ≈ 15 and 60 keV), event extraction was carried out using the FTOOLS task `hxdpinxbpi`. This extracts spectral counts, corrects for deadtime, and also returns a background spectrum which incorporates a typical contribution of the cosmic X-ray background component to the 'tuned' background model provided by the *Suzaku* team. Note that we used the latest version 2.2 (2.2ver1403) processing files which provide a more accurate estimate of the tuned non X-ray background for observations after 2012 August.

The source is too faint to be detectable in the higher energy HXD/GSO array, which is not considered here.

3 RESULTS

3.1 *Swift*

Fitting the BAT range with a power law (PL) returns a photon index of $\Gamma = 1.67^{+0.37}_{-0.36}$, and a flux $F_{14-195} = 1.2^{+0.4}_{-0.3} \times 10^{-11}$ erg s^{-1} cm^{-2} where the flux errors are determined using the XSPEC `cflux` command.

3.2 *Suzaku*

The source is undetected in the HXD/PIN. The total PIN count rate (source+background) is 0.247 ± 0.002 (15–60 keV), corresponding to a flux of 2.4×10^{-10} erg s^{-1} cm^{-2} when using a simple PL to characterize the HXD band. The typical systematic uncertainty on the NXB reproducibility is about 3 per cent for long observations (Fukazawa et al. 2009) which results in an HXD/PIN

flux upper limit of $F_{15-60} \sim 7.3 \times 10^{-12}$ erg s^{-1} cm^{-2}. This limit is consistent with the *Swift*/BAT fitted model, which has a flux $F_{15-60} = 5.3 \times 10^{-12}$ erg s^{-1} cm^{-2}, and the PIN data are not included in the analysis hereafter.

The source is clearly detected in the XIS FI and BI detectors. The spectra are shown in Fig. 1. The net count rates over the full range of ~ 0.3–10 keV are $9.1(\pm 0.4) \times 10^{-3}$ counts s^{-1} (FI) and $1.4(\pm 0.1) \times 10^{-2}$ counts s^{-1} (BI), respectively.

3.3 Broadband modelling

Fitting a simple PL model shows excesses above and below 2 keV suggesting the presence of at least two separate components. Over the 2–10 keV range, we find that a hard PL with $\Gamma = 0.69 \pm 0.37$ and a 6.4 keV Fe Kα line at the source systemic redshift can characterize the spectral shape adequately with $\chi^2 = 42.5$ for 41 degrees of freedom (dof). The observed flux is $F_{2-10} = 2.4^{+0.3}_{-0.4} \times 10^{-13}$ erg s^{-1} cm^{-2} and the Fe line equivalent width EW $= 1.7^{+0.7}_{-0.4}$ keV. Such a flat spectral shape and strong Fe line are characteristic of reflection-dominated spectra as may be expected in CTAGN, so we proceeded to fit several standard models of reflection.

3.3.1 *Reflection models*

As a first attempt, we used the PEXRAV model (Magdziarz & Zdziarski 1995) to fit the reflection continuum. PEXRAV assumes a slab geometry with an infinite optical depth of the reflector. It does not model the corresponding fluorescence emission lines expected, so a Gaussian component with fixed rest-frame energy of 6.4 keV and width $\sigma = 50$ eV was included to simulate the strongest expected neutral Fe Kα line. A direct transmitted PL with normalization and photon index tied to those of PEXRAV was included separately and absorbed by both photoelectric absorption and Compton scattering associated with the torus using the ZPHABS and CABS models in XSPEC, respectively. The PEXRAV reflection continuum was assumed not to be absorbed by the torus, as may be expected if the reflection arises in the visible portions of the back face of the torus, for example. Solar abundances were assumed. This model is referred to as 'Model P'.

PEXRAV has historically been a popular model for fitting reflection spectra, and it is useful for comparison with published analyses

of other sources. But since it does not self-consistently include fluorescence emission and requires ad hoc assumptions about the visible reflector solid angle, we also fitted more physically self-consistent reflection models MYTORUS (Murphy & Yaqoob 2009, hereafter 'Model M') and TORUS (Brightman & Nandra 2011, hereafter 'Model T'). These models both describe photoelectric absorption, Compton scattering and fluorescence iron emission from a toroidal gas structure centred on the AGN. There are differences between the two models which allow an investigation of the systematics associated with the unknown geometry of the obscurer. Whereas the geometry assumed by MYTORUS is a doughnut shape, with a line-of-sight column density $N_H(los)$ tied to the inclination angle (θ_{inc}) and the equatorial column $N_H(eq)$, TORUS takes a conical section of a sphere with $N_H(los)$ being independent of θ_{inc} for any line-of-sight passing through the torus. MYTORUS assumes a fixed covering factor of 0.5, whereas this is allowed to vary in TORUS through a variable opening angle θ_{tor}. MYTORUS allows the direct component to be decoupled from the scattered (MYTORUSS) and fluorescence (MYTORUSL) components and investigated independently of each other, whereas TORUS does not. Tabulated models are publicly available for both models up to column densities of $N_H(eq) = 10^{25}$ cm^{-2} (for MYTORUS) and $N_H = 10^{26}$ cm^{-2} (for TORUS), respectively. Neither of the two models include an exponential cutoff to the incident AGN PL whose energy would be related to the temperature of the hot electron corona. TORUS is valid up to an energy of 320 keV, whereas several tables with a variety of termination energies are available for MYTORUS. Here we used the tables valid up to 500 keV consistent with the energy coverage of our observed spectra as well as with the TORUS energy range. Both models assume solar abundances.

3.3.2 Additional model components

With an angular resolution of 2 arcmin (half-power diameter), *Suzaku* cannot resolve out X-rays emitted by sources other than the direct AGN emission and torus reflection. These sources include emission from extended gas photoionized by the AGN, thermal emission from a hot interstellar medium, intrinsic AGN emission that is scattered from reflecting media above the torus and emission from other point sources such as X-ray binaries. These sources may all dominate at low energies, typically below ~2 keV where the direct AGN emission is completely absorbed. Distinguishing between these various sources generally requires high spectral resolution and high-sensitivity soft X-ray data (e.g. Guainazzi & Bianchi 2007). In the absence of such data, we simply parametrized the soft X-rays regime using a thermal model with the APEC code (Smith et al. 2001) in conjunction with a scattered PL (with scattering fraction f_{scatt} relative to the intrinsic AGN continuum), and discuss its feasibility in the Discussion section. These were added to all three reflection models described above. Note that the spectral portions between energies of 1.7–1.9 keV and 2.1–2.3 keV are ignored because of instrumental calibration uncertainties related to the Si and Au edges. Finally, fixed Galactic absorption of 1.1×10^{21} cm^{-2} (Dickey & Lockman 1990) was also included in all spectral fits.

The XSPEC notation used to describe the three models is as follows, with explanatory associations in square brackets:

$$\text{MODEL P} = \text{CONST} \times \text{PHABS}[\mapsto N_H^{Gal}] \times (\text{APEC}$$
$$+\text{POW} * \text{CABS} * \text{ZPHABS}[\mapsto N_H(los)]$$
$$+\text{PEXRAV} + \text{ZGAUSS}$$
$$+\text{CONST}[\mapsto f_{scatt}] \times \text{POW}),$$

and

$$\text{MODEL T} = \text{CONST} \times \text{PHABS}[\mapsto N_H^{Gal}] \times (\text{APEC}$$
$$+\text{ATABLE}\{\texttt{torus1006.fits}\}$$
$$+\text{CONST}[\mapsto f_{scatt}] \times \text{POW}),$$

and

$$\text{MODEL M} = \text{CONST} \times \text{PHABS}[\mapsto N_H^{Gal}] \times (\text{APEC}$$
$$+\text{POW} * \text{ETABLE}\{\texttt{mytorus\_Ezero\_v00.fits}\}$$
$$+\text{ATABLE}\{\texttt{mytorus\_scatteredH500\_v00.fits}\}$$
$$+\text{ATABLE}\{\texttt{mytl\_V000010nEp000H500\_v00.fits}\}$$
$$\text{CONST}[\mapsto f_{scatt}] \times \text{POW}).$$

3.4 Combined *Suzaku* and *Swift* fits

The *Swift*/BAT observation provides a long-term average of the source flux. The *Suzaku* HXD/PIN flux limit is consistent with the *Swift*/BAT detected flux over 15–60 keV, meaning that the source could not have brightened significantly during the *Suzaku* observation with respect to the long-term average. We cannot rule out source fading, though CTAGN are generally dominated by reflection and variability is mitigated on light travel times across the torus. We thus fitted the *Suzaku* and *Swift* data simultaneously, accounting for flux variability and cross-calibration uncertainties using a scalar (CONSTANT) parameter C_{XIS}^{BAT} in the fits. This is fixed to 1 for the XIS FI and allowed free to vary for XIS BI as well as BAT. An important caveat to be kept in mind is that we cannot rule out a 'changing-look' nature with significant spectral variability using this approach.

Fig. 2 shows results of the fits for the three reflection models that we attempted, and the best-fitting parameters are listed in Table 1. Model P yields an acceptable fit with a column density $N_H(los) \approx 1.4 \times 10^{24}$ cm^{-2} that is borderline Compton thick. The data quality is not high enough to constrain θ_{inc} and the reflection fraction parameter R. The latter was fixed at $R = -1$ which is equivalent to a geometry where half of the intrinsic AGN emission is reflected, as may be expected for a sky covering factor of 0.5 for the torus. The fits prefer a near edge-on inclination model limit of $\cos(\theta_{inc}) = 0.05$, though this is formally unconstrained. The fitted AGN photon index of $\Gamma = 1.9$ is quite typical of bright well-studied local AGN (e.g. Mateos et al. 2005; Piconcelli et al. 2005). The high Fe line EW($K\alpha$) ≈ 1 keV is fully consistent with a Compton-thick absorbing column. However, there is a clear offset between the XIS and BAT with the cross-normalization constant of BAT relative to XIS being significantly larger than 1, and possibly much larger than 2. This could be caused by flux variability as the two data sets are not strictly simultaneous. But it could also be related to the limitations of the PEXRAV model. Since this model does not self-consistently model the fluorescence emission strength, and since the transmitted and reflected components (likely dominating above and below 10 keV, respectively) are decoupled, there can be significant degeneracy when fitting non-simultaneous data covering non-overlapping energy ranges. In fact, as we show below, use of the more physical torus reflection models do not require large cross-calibration factors.

We first considered the TORUS model T. The fitted intrinsic continuum PL has a photon index $\Gamma = 2.1$ and is absorbed by a high column density of $N_H > 1.6 \times 10^{24}$ cm^{-2} consistent with being Compton thick at 90 per cent confidence. The upper N_H limit
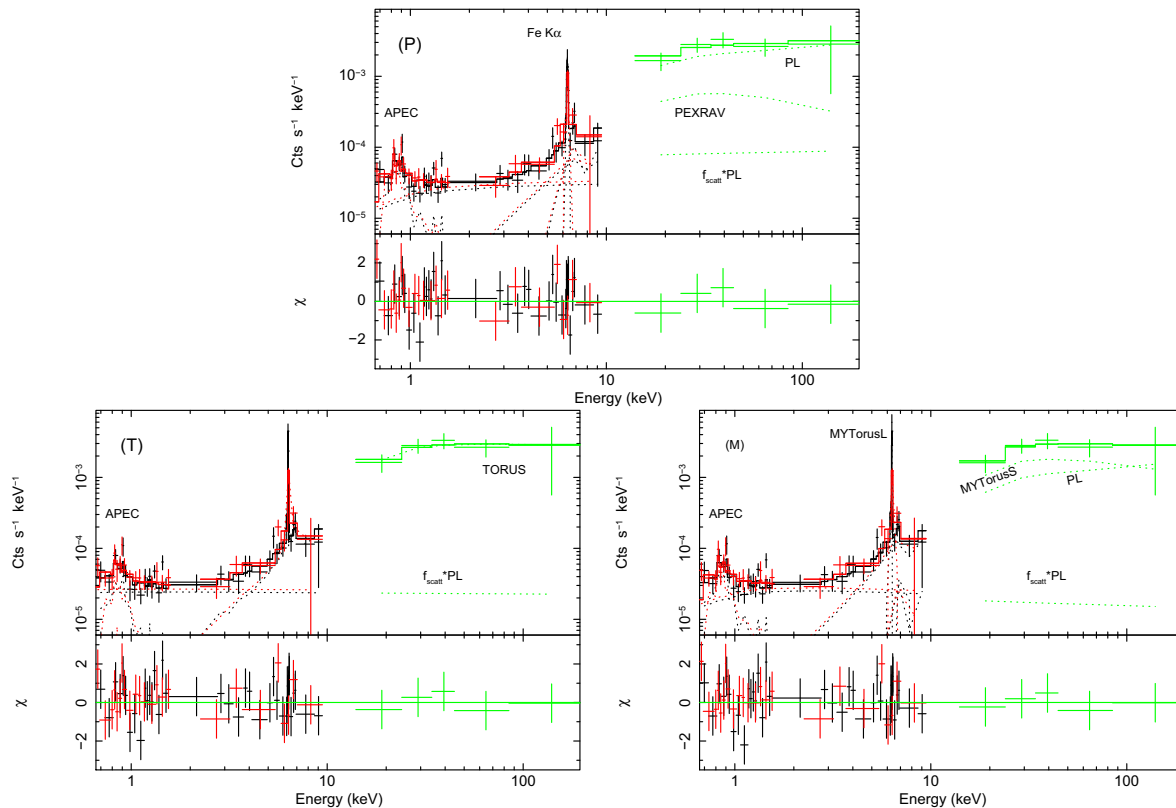
Figure 2. Broadband fits of models P (Top), T (Left) and M (Right) to the combined *Suzaku* and *Swift* spectrum of NGC 4785. The panels show the unfolded models in EF_E units. Residuals in units of sigmas are shown in the panels at the bottom. The APEC component dominates at the softest energies, and the scattered PL over $\approx$1–4 keV. In models P and M, the contributions of the direct absorbed PL (peaking around 150 keV), the Compton-scattered torus emission (peaking around 30 keV) and the fluorescence emission lines are separated. The TORUS model (Model T) does not distinguish these contributions and only the total emission of the torus is plotted.

Table 1. Results of X-ray spectral fitting to NGC 4785.

Component	Parameter	Model P	Model T	Model M	Units
APEC	kT	$0.68^{+0.08}_{-0.10}$	$0.69^{+0.09}_{-0.10}$	$0.68^{+0.03}_{-0.02}$	keV
Absorber/Reflector	$N_{\rm H}$(eq)	–	–	$2.9^{+4.1}_{-0.8}$	$\times 10^{24}$ cm^{-2}
	$N_{\rm H}$(los)	$1.4^{+0.5}_{-0.9}$	$2.2^{+u}_{-0.6}$	$2.7^{+3.8}_{-0.8}$	$\times 10^{24}$ cm^{-2}
	$\theta_{\rm inc}$	87^{+u}_{-u}	87^{+u}_{-50}	79^{+6}_{-15}	deg
	$\theta_{\rm tor}$	–	56^{+25}_{-u}	–	deg
	R	-1^f	–	–	
	EW(Fe Kα)	$1.1^{+u}_{-0.4}$	c	c	keV
AGN continuum	Γ	$2.0^{+0.4}_{-0.4}$	$2.1^{+0.3}_{-0.4}$	$2.1^{+0.5}_{-0.4}$	
Diffuse Scattering	$f_{\rm scatt}$	$14.8^{+280}_{-9.9}$	$4.2^{+9.0}_{-4.1}$	$2.2^{+7.5}_{-2.0}$	$\times 10^{-3}$
$C^{\rm XIS\ BI}_{\rm XIS\ FI}$ cross-calib	CONST	$1.11^{+0.19}_{-0.16}$	$1.10^{+0.18}_{-0.16}$	$1.10^{+0.18}_{-0.16}$	
$C^{\rm BAT}_{\rm XIS\ FI}$ cross-calib	CONST	$2.48^{+5.32}_{-0.99}$	$1.07^{+1.10}_{-0.47}$	$0.85^{+1.11}_{-0.54}$	
χ^2/dof		78.5/88	76.7/88	76.5/89	

^{u}Unconstrained. ^{f}Fixed. ^{c}Line is produced self-consistently in the model.
Model P: PEXRAV component fit (Magdziarz & Zdziarski 1995).
Model M: MYTORUS coupled component fit (Murphy & Yaqoob 2009).
Model T: TORUS model component fit (Brightman & Nandra 2011).

is unconstrained, with the model threshold of $N_{\rm H} = 10^{26}$ cm^{-2} allowed. The Fe line is treated self-consistently in the TORUS model as fluorescence from the torus. In order to gauge the line strength separately, we fitted an ad hoc model with a PL continuum fixed to an approximation of the continuum fitted by the

TORUS model between energies of 5.5 and 7.0 keV (excluding the line), and then overlaid a Gaussian component to model the Kα line. For the XIS FI data, this yielded EW(Kα) $\approx$ 0.8 keV. Allowing the continuum level to vary increases the line strength to EW(Kα) $\approx$ 1.0 keV.

The cross-normalization constants between the XIS FI and BI, and also between XIS FI and BAT, are both consistent with 1 within the uncertainties, though a factor of up to ≈ 2 variation between BAT and XIS cannot be excluded. θ_{inc} is largely unconstrained, ranging over ≈ 40–87.1 deg, the latter being the upper threshold allowed in the model. Model solutions at both the low and the high end of this range appear to be equally preferred, and we used the solution at the high end, because it allows for the full range of θ_{tor} values to be investigated (Brightman & Nandra 2011). However, we did not fix θ_{inc} to an edge-on inclination because there may be some discrepancy at the low-energy end of the model for these configurations (Liu & Li 2015). We do not expect the results to change drastically at the higher energies where most of the reflection features originate, however, especially for the moderate data quality spectra available here. We confirmed this by trying a variety of fixed inclination angles and obtained largely consistent results for the main parameters of interest including N_H(los) and L_{2-10} discussed later. In addition, the results are broadly consistent with the MYTORUS model below.

We find that θ_{tor} values down to the lowest allowed model threshold of 26 deg are allowed. But $\theta_{tor} > 80$ deg are excluded. The scattered PL fraction (f_{scatt}) is constrained to be small below ~ 1 per cent. Note that we fixed the photon index of the scattered component to be the same as that of the intrinsic AGN PL. The temperature of the APEC component is ~ 0.7 keV in all three models, although an alternate solution at $kT \approx 0.2$ keV was also allowed in model T for the lower range of θ_{inc} quoted above.

We next tried replacing the torus reflection component with the simplest version of MYTORUS (model M) which couples the normalizations and column densities of the scattered and fluorescence components to the zeroth-order absorption distortion model of the direct continuum. The softer APEC and scattered components were included as before. As seen in Fig. 2 and Table 1, this can yield a fit as good as Model T, again with a Compton-thick obscurer solution with N_H(los) = (2–7) $\times 10^{24}$ cm^{-2}. The opening angle of the torus is effectively fixed in the coupled MYTORUS model, and a broad range of inclination angles $\theta_{inc} = 64$–85 deg is allowed.

4 DISCUSSION

We have presented the first pointed X-ray observations of NGC 4785, taken in 2013. The source has long been known as a relatively nearby Sy 2, but little is known of the intrinsic AGN properties. With *Suzaku*, in combination with *Swift*/BAT, we show the source to be obscured by a line-of-sight gas column that is consistent with being Compton-thick during the observation. This is based upon broad-band X-ray spectral modelling over the range of ≈ 0.3–195 keV and the detection of a prominent neutral Fe Kα emission line, both of which can be self-consistently fitted with the latest models incorporating Compton scattering off toroidal obscurers.

4.1 Broadband spectral components

The obscuring column density along the line-of-sight is constrained to be greater than 1.5×10^{24} cm^{-2} for both the torus models that we tried, and near Compton thick in the PEXRAV model. Although all three models are approximately consistent, the fits described in the previous section demonstrate that the physical torus models can effectively produce more spectral curvature than PEXRAV, and can fit both the XIS and BAT regimes without the need for large cross-calibration factors. Furthermore, unlike PEXRAV, these models

self-consistently produce fluorescence emission. Therefore, for the remainder of this paper, we concentrate on the results of the torus models.

Model M demands $N_H \approx (2$–7) $\times 10^{24}$ cm^{-2}. For model T, the N_H upper limit is apparently unconstrained with values as high as the model threshold of $N_H = 10^{26}$ cm^{-2} allowed. But examining these solutions with extreme N_H values shows that they require a significant mismatch between the *Suzaku* and *Swift* flux levels, with the cross-normalization constant $C_{XIS\ FI}^{BAT}$ being ≈ 2. Although such strong variability cannot be completely ruled out, it is unlikely for a highly obscured AGN with distant reflection washing out rapid and strong fluctuations. Restricting the $C_{XIS\ FI}^{BAT}$ to within 20 per cent of unity (say) and carrying out the fit to model T yields $N_H \approx (2$–9) $\times 10^{24}$ cm^{-2}. We also note that we have not attempted more complex models such as the decoupled MYTORUS configuration which allows greater flexibility in setting the line-of-sight and global torus properties independently. The present data quality is not high enough to warrant models with many more degrees of freedom. In particular, it will be very useful to have contiguous broad-band coverage without a data gap around 10 keV in order to mitigate instrument cross-calibration uncertainties. These issues can be better investigated with data from *NuSTAR* (Harrison et al. 2013) and *ASTRO-H* (Takahashi et al. 2012).

The soft band luminosity of the APEC component is $L_{0.5-2} = 1.6 \times 10^{40}$ erg s^{-1} (corrected for Galactic absorption). The luminosity of the hot thermal gas in the host galaxy described by APEC should be related to the star formation rate (SFR). Using the relation of Mineo, Gilfanov & Sunyaev (2012), we find $SFR_{X-ray} = 30^{+37}_{-16}$ M$_\odot$ yr^{-1} (1σ scatter). This can be compared with the SFR measured in the far-infrared. NGC 4785 was detected by the *IRAS* mission with a bolometric (8–1000 µm) luminosity $L_{8-1000} = 5 \times 10^{10}$ L$_\odot$ (2×10^{44} erg s^{-1}), based upon the 12–100 µm fluxes in the *IRAS* Faint Source Catalogue v2.0 (Moshir et al. 1990) and equations from Sanders & Mirabel (1996). Using the far-infrared luminosity versus SFR relation by Kennicutt (1998), we find $SFR_{IR} = 9$ M$_\odot$ yr^{-1}. This is close to the lower 1σ limit implied by SFR_{X-ray} and a star formation contribution to both the infrared and soft X-rays appears viable. However, it should be noted that high spectral resolution and high sensitivity observations have shown AGN photoionization to dominate the soft X-ray emission of nearby Seyferts (e.g. Sako et al. 2000; Kinkhabwala et al. 2002; Guainazzi & Bianchi 2007). A complex of photoionization lines can mimic a thermal spectrum in low spectral resolution data, and in such a case, the soft X-ray contribution related to star formation could decrease and become consistent with the far-infrared. Such a scenario would also affect the level of the scattered component that dominates over energies of ≈ 1–4 keV, and there is some degeneracy between these components. The best way to distinguish between the various physical models for the soft X-ray emission is through high spectral resolution observations, e.g. using the Soft X-ray Spectrometer which will soon be available on board *ASTRO-H* (Takahashi et al. 2012).
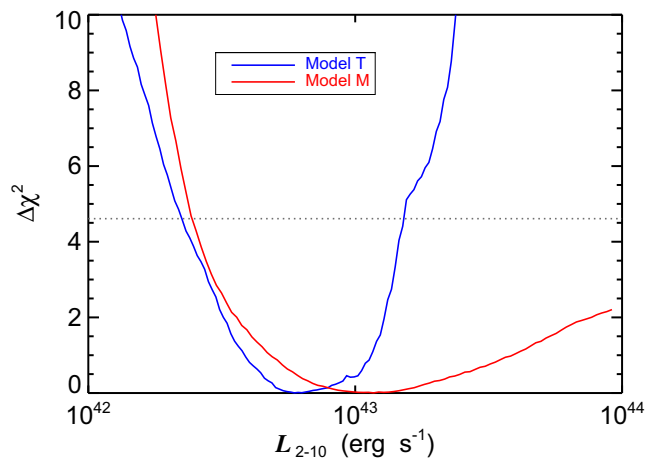
4.2 AGN luminosity

The *observed* (absorbed) 2–10 keV AGN luminosity of NGC 4785 is $L_{2-10}^{obs} = 1.1 \times 10^{41}$ erg s^{-1}. The intrinsic luminosity must be higher but is largely unknown, even from indirect diagnostics that are often used as bolometric AGN luminosity indicators. These diagnostics include the [O III]λ 5007 Å emission line (e.g. Panessa et al. 2006) and the hot dust AGN emission (e.g. the 12 µm nuclear continuum luminosity; Gandhi et al. 2009). Absolute optical

emission line fluxes have not been published, to our knowledge. In the infrared, one may use data from the *WISE* all sky survey (Wright et al. 2010). The latest AllWISE catalogue[5] (Cutri et al. 2013) tabulates pipeline-measured magnitudes based upon profile-fitting on ~ 6 arcsec scales. The public *WISE* catalogues also provide aperture photometry measurements which would include large scale host galaxy emission, but the profile fitting magnitudes provide better constraints on emission from the nuclear regions alone. These fits do assume a point source profile, but can optimally handle masked pixels and are free from artefacts such as saturation.[6] We used the standard zero-point from Jarrett et al. (2011) and find a monochromatic 12 μm luminosity in the *W*3 band (which has a central wavelength closest to 12 μm) of 7.2×10^{42} erg s^{-1}. This is to be regarded as an upper limit of the monochromatic AGN power given that there is likely to be at least some non-AGN contamination. In fact, as we discuss later, the *WISE* fluxes are very unlikely to be AGN dominated.

NGC 4785 is also included in the large atlas of high angular resolution mid-infrared (hereafter mid-IR) imaging compiled by Asmus et al. (2014) where the nucleus is a non-detection on sub-arcsec scales with a luminosity upper limit $L_{12} \equiv \lambda L_\lambda$ (12 μm) $< 2 \times 10^{42}$ erg s^{-1}. This flux is an extrapolated estimate based upon a single VLT/VISIR (Lagage et al. 2004) filter observation in the PAH2 band centred on 11.25 μm in the observed frame. The observation was aborted before completion, resulting in a prominent pattern in the background across the image. We checked that such artefacts should not adversely affect the photometry drastically, though multiband photometry is required to unambiguously prove this to be the case. There is no mid-IR spectrum of the source available so it is unknown if there is a strong silicate absorption feature affecting this band.

In X-rays, the intrinsic AGN flux is simply the integral of $AE^{1-\Gamma}$ over the energy range of interest, with Γ being the fitted photon index and A the normalization. However, constraining the intrinsic PL flux level of CTAGN can be subject to great uncertainty given the unknown geometry of the absorber (e.g. Yaqoob 2012). Most studies of CTAGN do not quote errors on the intrinsic luminosity, or use the uncertainty on the normalization alone as an error on the luminosity for simplicity, not accounting for the joint variation of Γ. As a result, the uncertainty on the luminosity may be severely underestimated.

Here, we measure realistic luminosity uncertainties by computing the joint 90 per cent confidence contours on the two interesting parameters of A and Γ. The 90 per cent confidence interval on the intrinsic flux (and thus luminosity) is then computed from the flux for all sets of parameters that lie within this 90 per cent confidence region. Fig. 3 shows the resultant relative χ^2 values for various values of L_{2-10} (i.e. various combinations of A and Γ). It is clear that there is large uncertainty in L_{2-10}. For model T, the 90 per cent range corresponding to a $\Delta\chi^2 = 4.61$ for two interesting parameters spans $\approx 2 \times 10^{42}$ to 2×10^{43} erg s^{-1}. Model M turns out to be even less constraining with luminosities above 10^{44} erg s^{-1} allowed. Fixing Γ at a value of 1.9 corresponding to the mean observed in well-sampled AGN spectra (Mateos et al. 2005; Piconcelli et al. 2005), we find $L_{2-10} = 4.7^{+9.4}_{-1.7} \times 10^{42}$ erg s^{-1} (model T) and $L_{2-10} = 8.7^{+120}_{-7.0} \times 10^{42}$ erg s^{-1} (model M), respectively, with the error in these cases being determined by the normalization uncertainties alone.

[5] http://wise2.ipac.caltech.edu/docs/release/allwise
[6] wise2.ipac.caltech.edu/docs/release/allsky/expsup/sec4_4c.html

Figure 3. The intrinsic PL luminosity uncertainty for models T and M, computed by fitting over a grid of PL photon index and normalization values. The dotted line corresponds to a $\Delta\chi^2 = 4.61$ equivalent to a 90 per cent interval for two interesting parameters.

These X-ray luminosities are consistent with known infrared: X-ray luminosity relations for Seyferts (e.g. Horst et al. 2008; Gandhi et al. 2009; Asmus et al. 2011) within the large present uncertainties, though the VLT and *WISE* luminosities quoted above prefer the lower end of the allowed X-ray range. For example, using the L_{2-10} versus L_{12} relations by Gandhi et al. (2009) with the *WISE* luminosity predicts $L_{2-10} = (3-5) \times 10^{42}$ erg s^{-1}. Using the VLT/VISIR upper limits instead, the predicted luminosities are $L_{2-10} < (0.9-2) \times 10^{42}$ erg s^{-1} which are in light tension with the 90 per cent confidence intervals of L_{2-10} from models M and T. This may be a sign of mild anisotropy in the mid-IR emission of the obscuring torus (e.g. Hönig et al. 2011). Such anisotropies appear to be a generic feature of smooth as well as clumpy models resulting from stochastic distributions of torus cloud geometries (e.g. Feltre et al. 2012). Alternatively, there may be intrinsic differences in the cloud distributions of Seyfert 1s versus Seyfert 2s (Alonso-Herrero et al. 2011; Ramos Almeida et al. 2011). Deep multiband sub-arcsec photometry will be able to test these various hypotheses, as will obtaining a mid-IR spectrum to search for any absorption related to the silicate feature.

One may also make comparisons to the relations of Matsuta et al. (2012) and Ichikawa et al. (2012) which are defined between *AKARI* MIR bands and the BAT X-ray bands and should be largely unaffected by photoelectric absorption, with Compton scattering being the main determinant of any X-ray offsets. For NGC 4785, $L_{14-195} = 5.0^{+1.7}_{-1.2} \times 10^{42}$ erg s^{-1}. NGC 4785 is not catalogued in the MIR *AKARI* all-sky survey (Ishihara et al. 2010) so we convert its *WISE* W3 power to the equivalent 9 μm *AKARI* luminosity by using equation 2 from Ichikawa et al. (2012), which yields $L_9 = 8.2 \times 10^{42}$ erg s^{-1}. These luminosities place NGC 4785 very close to the L_9–L_{BAT} relation reported by Matsuta et al. (2012). It should be noted that this relation is for observed BAT luminosities, uncorrected for the effects of Compton scattering. The modelled N_H values for model M (Table 1) introduce Compton scattering corrections of up to a factor of a few, small enough that the source would lie very close to the L_9–L_{BAT} relation and well within the relation scatter reported by Matsuta et al. (2012). One reason for this apparent discrepancy in the position of the source with respect to the L_9–L_{BAT} and the L_{12}–L_{2-10} relations is simply that the scatter in the reported *AKARI*–BAT relations is larger than found using high
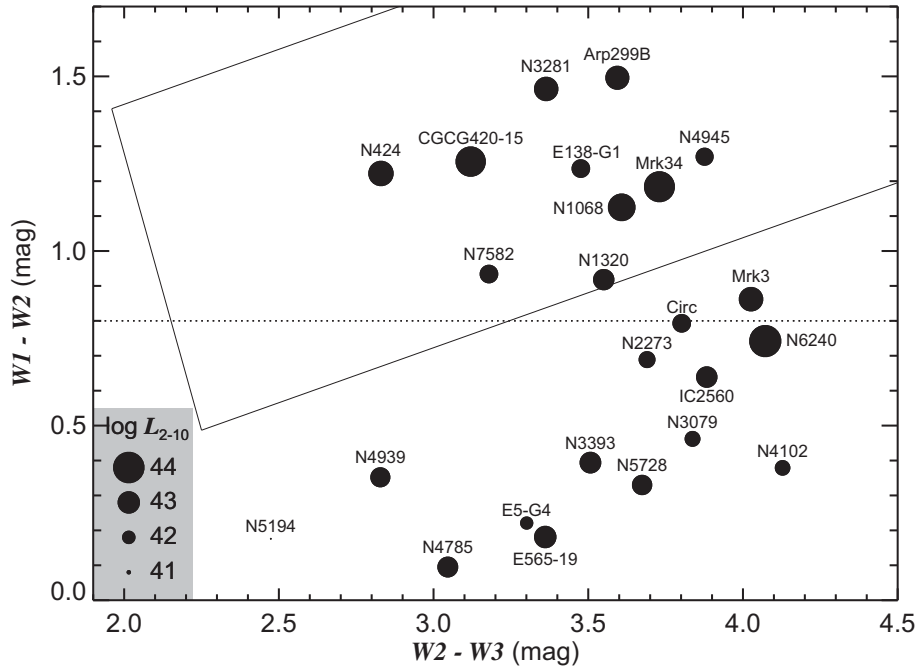
Figure 4. *WISE* colour–colour plot showing NGC 4785 and all known bona fide CTAGN from Gandhi et al. (2014). The 'AGN wedge' from Mateos et al. (2012) and the colour cut from Stern et al. (2012) are shown with the continuous and dashed lines, respectively. Profile-fitting photometry from the AllWISE data base is used here, except for Mrk 3 where the three-band Post-Cryo *WISE* catalogue is used because there is no reported *W3* flux in the AllWISE data base. The sizes of the symbols scale with logarithmic intrinsic 2–10 keV power (size key on the lower left). Median 1σ errors on the colours are approximately 0.03 mag, except for larger errors in the case of two sources with saturated *WISE* photometry NGC 1068 and Circinus. No correction is made for this minor effect, as this is not relevant for the discussion here.

angular resolution MIR data by Gandhi et al. (2009). Another is that stellar contamination to the *WISE* (and hence derived *AKARI*) fluxes is not resolved out, unlike the high angular 12 μm measurements used by Gandhi et al. (2009). However, still another possibility may be that the Compton scattering correction factors have been overestimated in our X-ray fits. The 2–10 keV band is more sensitive to high column density corrections, which may result in a stronger overcorrection in this band. This could be the case if, for instance, the source is a changing-look AGN with a very small covering factor of Compton-thick clouds. Our X-ray fits with physical torus models instead assume a torus with typical covering factors and corresponding typical corrections from the observed reflection component to the intrinsic power. Follow-up X-ray monitoring will easily clarify if the source is a changing-look AGN.

Another potential proxy of the intrinsic luminosity is provided by nuclear water masers. A possible relation between AGN power and masing luminosity has been published by Kondratko, Greenhill & Moran (2006), with L_{2-10} being a proxy of the AGN power driving the maser. Braatz, Wilson & Henkel (1996) carried out H_2O maser observations of NGC 4785 and show that the source is undetected down to an isotropic luminosity $L_{H_2O} \lesssim 4\,L_\odot$ (1-σ). A 3σ limit, together with the Kondratko et al. (2006) relation, would predict $L_{2-10} \lesssim 7 \times 10^8\,L_\odot$ (3 × 10^{42} erg s^{-1}) though a factor of a few higher luminosity is allowed by the relation scatter.

In summary, our X-ray modelling shows that L_{2-10} lies above $\approx 2 \times 10^{42}$ erg s^{-1} for both models M and T at 90 per cent confidence. At the upper end, model T lies below $L_{2-10} \approx 2 \times 10^{43}$ erg s^{-1}, whereas model M is much less constrained and allows values above 10^{44} erg s^{-1}. However, two other proxies of the AGN power (the 12 μm continuum and the water maser power) both prefer the lower end of the allowed L_{2-10} range. As a con-

servative X-ray estimate, we therefore use the range of uncertainty found from model T, i.e. a 1 dex interval of $L_{2-10} \approx 2 \times 10^{42}$– 2×10^{43} erg s^{-1}. Measurement of the [O III] narrow emission line luminosity will provide an additional indirect diagnostic on the intrinsic power, as will direct sensitive broad-band X-ray spectroscopy with *NuSTAR*.

4.3 Comparison to other bona fide CTAGN

Follow-up pointed X-ray observations will be important for confirming whether the source is a steady, bona fide CTAGN, or whether it has a changing-look nature (Section 4.2). But it is interesting to ask how NGC 4785 is placed in the context of known bona fide CTAGN. Fig. 4 shows the distribution of bona fide CTAGN as compiled by Gandhi et al. (2014, and references therein) on the canonical *WISE* colour–colour plane. Increasing levels of AGN contribution to the mid-IR fluxes (relative to the stellar host galaxy contribution) have been shown to move objects approximately upwards in this plot, with most AGN-dominated sources found above the colour cut of $W1 - W2 = 0.8$ proposed by Stern et al. (2012) and also within the AGN wedge proposed by Mateos et al. (2012). It is clear from the plot that the bona fide CTAGN population is quite heterogeneous in its mid-IR colour distribution, with about half of the sources lying below the AGN wedge and cut thresholds. In general, more luminous Seyferts are able to dominate the observed mid-IR fluxes (see also Asmus et al. 2014) and so lie above the thresholds. However, not all sources outside the AGN wedge are intrinsically weak (e.g. NGC 6240 and Mrk 3). NGC 4785 shows a bluer $W1 - W2$ colour than all known bona fide CTAGN, despite the fact the AGN power is not especially weak in X-rays. This could result either from strong host star formation activity contributing
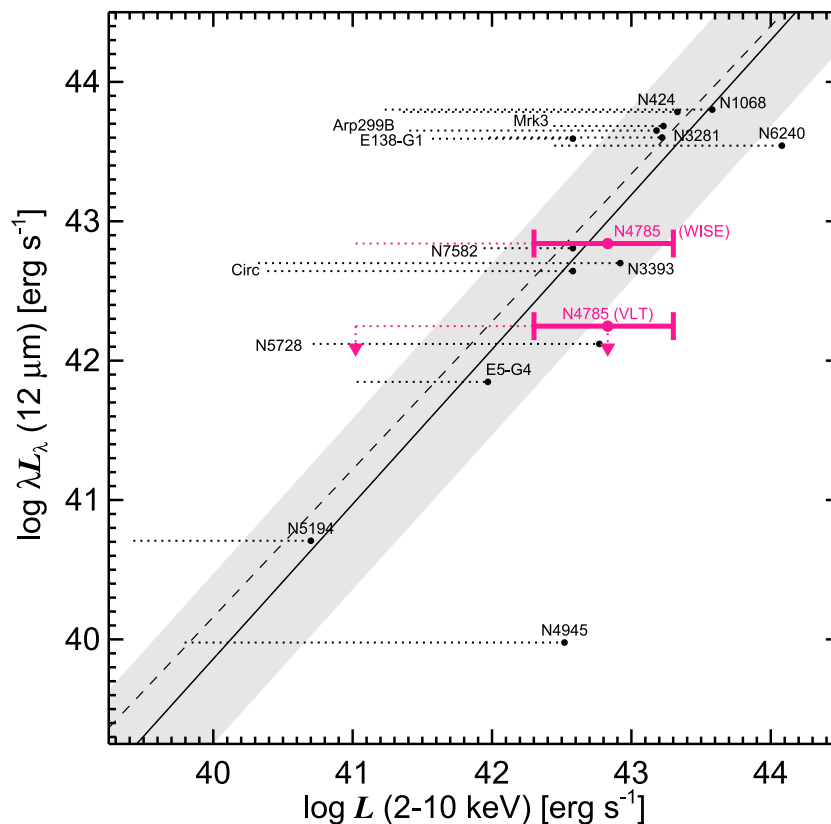
Figure 5. Mid-IR versus X-ray luminosity plot, showing the position of NGC 4785 in relation to known bona fide CTAGN with sub-arcsec 12 μm photometry from the high angular resolution mid-IR AGN atlas of Asmus et al. (2014). For each source, a dotted horizontal line connects the observed (absorbed) L_{2-10} on the left with the intrinsic (absorption-corrected) power on the right, the latter shown as a filled circle. The X-ray data are compiled in Goulding et al. (2012), Gandhi et al. (2014), and references therein. The solid line is the mid-IR versus X-ray relation from Gandhi et al. (2009) with the shaded region being the 2σ relation scatter. For comparison, the dashed line shows a different version of the relation from Asmus et al. (2011, fitted to include low luminosity AGN). For NGC 4785, two mid-IR luminosities are plotted: the detection is from *WISE* and the upper-limit denoted by arrows is from the VLT. A horizontal bar is shown in both cases spanning the 90 per cent uncertainty on the intrinsic X-ray luminosity.

to the mid-IR, or from anisotropic and/or weak reprocessed torus emission. Detailed modelling of the broad-band spectral energy distribution (SED) will be required to distinguish between these scenarios, which is beyond the scope of this work. The high SFR values derived in Section 4.1 would support an elevated host galaxy stellar dilution to the mid-IR. This would also be consistent with the results of Mateos et al. (2013), who have shown that CTAGN have *WISE* colour distributions similar to Compton-thin ones. In their work, the main determinant of the position of any source in the *WISE* colour space is the contrast between AGN and host MIR emission.

However, the non-detection of the nucleus in high angular resolution imaging by Asmus et al. (2014) could instead support an atypical SED for NGC 4785. This is shown in Fig. 5, which includes the 15 bona fide CTAGN with mid-IR photometry in the Asmus et al. (2014) atlas. The absorbed and the intrinsic X-ray luminosities for each source are compared to sub-arcsec 12 μm photometry. Correction for absorption places almost all sources close to the mid-IR versus X-ray relation derived for a local sample of Seyfert galaxies by Gandhi et al. (2009). NGC 4945 is the strongest known outlier, being underluminous in the mid-IR by about two orders of magnitude for its X-ray power according to the figure (its offset from the relation is also discussed in Krabbe, Böker & Maiolino 2001; Levenson et al. 2009; Asmus et al., in preparation). In fact, this source is known to be a uniquely prominent outlier in terms of

many of its properties, including showing weak and absent coronal lines (Goulding & Alexander 2009), potentially possessing a fully embedded AGN (Done et al. 2003) and a putative obscuring torus with atypically low covering factor (e.g. Madejski et al. 2000; Itoh et al. 2008; Puccetti et al. 2014). Much of the X-ray reflection signatures usually attributed to a circumnuclear torus instead appear to originate in clouds on much large scales associated with a starburst ring (Marinucci et al. 2012), which may result in lack of hot dust in the immediate AGN environment. Finally, part of its mid-IR decrement with respect to the mid-IR:X-ray relation may also be related to the edge-on orientation of its host galaxy, with its strong 10 μm silicate absorption feature arising on host galaxy scales (Goulding et al. 2012).

NGC 4785 is also underluminous with respect to the mid-IR: X-ray relation, but only mildly based upon the present mid-IR upper-limit (and with the aforementioned caveat about the unknown contribution of silicate absorption in the high angular resolution data). The inclination angle of the host galaxy is 65.5 deg according to the HyperLEDA data base,[7] and there are no obvious signatures of dust lanes in archival optical and near-IR imaging, so this is clearly a different configuration as compared to NGC 4945. However, the core of NGC 4785 has been found to possess a complex structure,

[7] http://leda.univ-lyon1.fr

showing a bright thick double bar as well as an inner disc on scales of ∼0.3–3 kpc (Márquez et al. 1999; Erwin 2004). Mapping the nuclear extinction and cold dust content (e.g. with multiband optical, infrared and sub-mm observations) will shed more light on the magnitude of large-scale obscuration related to the host galaxy, as will obtaining a mid-IR spectrum to search for silicate absorption.

In any case, it is clear that if there is a large population of other such CTAGN, they will not be identified easily in the mid-IR alone, even through analyses of the multiband SEDs, as their AGN mid-IR signatures are sub-dominant. Infrared coronal lines such as the [Ne v] λ 14.3 µm line are excellent AGN indicators (Weaver et al. 2010; Meléndez et al. 2011; Goulding et al. 2012; Annuar et al., in preparation), but infrared spectroscopy is highly time-intensive. All-sky X-ray surveys (either with the deepening *Swift*/BAT survey above 10 keV, or with the upcoming SRG/e-ROSITA mission below 10 keV; Merloni et al. 2012) combined with broad-band X-ray modelling may be the best way to uncover this population of sources. The samples used to define the already published mid-IR:X-ray relations (e.g. Krabbe et al. 2001; Lutz et al. 2004; Gandhi et al. 2009; Levenson et al. 2009; Asmus et al. 2011) do include other edge-on systems, barred and dusty galaxies, and it is not obvious that a significant population of such sources has been missed thus far, but this remains an issue to be investigated with larger complete samples.

Finally, we note that the presence of Compton-thick obscuration has been linked to the presence of stellar host galaxy bars (Maiolino, Risaliti & Salvati 1999), and NGC 4785 appears to support this link. Of the 24 CTAGN in Fig. 4 (the 23 bona fide sources from Gandhi et al. 2014, plus NGC 4785) with detailed morphological studies, 11 have known bars according to the HyperLEDA data base. Another two lie in edge on systems, where a bar may be difficult to identify. This suggests that 11 of 22, or 50^{+24}_{-18} per cent of bona fide CTAGN are associated with barred hosts.[8] The overall fraction of spiral galaxies with bars is known to be a strong function of stellar mass (Nair & Abraham 2010), with a value of $\approx$ 0.25–0.3 (or 25–30 per cent) for galaxies with a stellar mass of a few times 10^{10} M$_\odot$ that should be typical for local hard X-ray-detected AGN (Koss et al. 2011). So there appears to be an excess of CTAGN in barred hosts as compared to the overall galaxy population with bars. However, bar identification has many caveats. For instance, it has been shown that the bar fraction determined from infrared imaging is about twice as high as when using optical imaging (Eskridge et al. 2000). Therefore, caution is required when interpreting this result, and a detailed assessment of the significance and cause of this suggestive link will be important for understanding the heterogeneity in CTAGN properties.

ACKNOWLEDGEMENTS

REFERENCES

Akylas A., Georgakakis A., Georgantopoulos I., Brightman M., Nandra K., 2012, A&A, 546, A98

Alonso-Herrero A. et al., 2011, ApJ, 736, 82

Arévalo P. et al., 2014, ApJ, 791, 81

Arnaud K. A., 1996, in Jacoby G. H., Barnes J., eds, ASP Conf. Ser. Vol. 101, Astronomical Data Analysis Software and Systems V. Astron. Soc. Pac., San Francisco, p. 17

Asmus D., Gandhi P., Smette A., Hönig S. F., Duschl W. J., 2011, A&A, 536, A36

Asmus D., Hönig S. F., Gandhi P., Smette A., Duschl W. J., 2014, MNRAS, 439, 1648

Baloković M. et al., 2014, ApJ, 794, 111

Barthelmy S. D. et al., 2005, Space Sci. Rev., 120, 143

Baumgartner W. H., Tueller J., Markwardt C. B., Skinner G. K., Barthelmy S., Mushotzky R. F., Evans P. A., Gehrels N., 2013, ApJS, 207, 19

Blackburn J. K., 1995, in Shaw R. A., Payne H. E., Hayes J. J. E., eds, ASP Conf. Ser. Vol. 77, Astronomical Data Analysis Software and Systems IV. Astron. Soc. Pac., San Francisco, p. 367

Braatz J. A., Wilson A. S., Henkel C., 1996, ApJS, 106, 51

Brightman M., Nandra K., 2011, MNRAS, 413, 1206

Brightman M., Nandra K., Salvato M., Hsu L.-T., Rangel C., 2014, MNRAS, 443, 1999

Burlon D., Ajello M., Greiner J., Comastri A., Merloni A., Gehrels N., 2011, ApJ, 728, 58

Comastri A., Setti G., Zamorani G., Hasinger G., 1995, A&A, 296, 1

Cusumano G. et al., 2010a, A&A, 510, A48

Cusumano G. et al., 2010b, A&A, 524, A64

Cutri R. M. et al., 2013, Tech. Rep. Explanatory Supplement to the AllWISE Data Release Products, IPAC, Caltech, California

de Vaucouleurs G., de Vaucouleurs A., Corwin Jr . H. G., Buta R. J., Paturel G., Fouqué P., 1991, Third Reference Catalogue of Bright Galaxies. Volume I: Explanations and References. Volume II: Data for Galaxies Between 0^h and 12^h. Volume III: Data for Galaxies Between 12^h and 24^h. Springer, New York

Della Ceca R. et al., 2008, Mem. Soc. Astron. Ital., 79, 65

Dickey J. M., Lockman F. J., 1990, ARA&A, 28, 215

Done C., Madejski G. M., Życki P. T., Greenhill L. J., 2003, ApJ, 588, 763

Draper A. R., Ballantyne D. R., 2010, ApJ, 715, L99

Erwin P., 2004, A&A, 415, 941

Eskridge P. B. et al., 2000, AJ, 119, 536

Fabian A. C., Iwasawa K., 1999, MNRAS, 303, L34

Fairall A. P., 1986, MNRAS, 218, 453

Feltre A., Hatziminaoglou E., Fritz J., Franceschini A., 2012, MNRAS, 426, 120

Fukazawa Y. et al., 2009, PASJ, 61, 17

Gandhi P., Fabian A. C., 2003, MNRAS, 339, 1095

Gandhi P., Fabian A. C., Suebsuwong T., Malzac J., Miniutti G., Wilman R. J., 2007, MNRAS, 382, 1005

Gandhi P., Horst H., Smette A., Hönig S., Comastri A., Gilli R., Vignali C., Duschl W., 2009, A&A, 502, 457

Gandhi P. et al., 2013, ApJ, 773, 51

Gandhi P. et al., 2014, ApJ, 792, 117

Gehrels N., 1986, ApJ, 303, 336

Gehrels N. et al., 2004, ApJ, 611, 1005

Georgantopoulos I. et al., 2013, A&A, 555, A43

---

[8] 1σ uncertainties on the percentage are determined according to Gehrels (1986) and using error propagation.

Gilli R., Comastri A., Hasinger G., 2007, A&A, 463, 79

Goldwurm A. et al., 2003, A&A, 411, L223

Górski K. M., Hivon E., Banday A. J., Wandelt B. D., Hansen F. K., Reinecke M., Bartelmann M., 2005, ApJ, 622, 759

Goulding A. D., Alexander D. M., 2009, MNRAS, 398, 1165

Goulding A. D., Alexander D. M., Bauer F. E., Forman W. R., Hickox R. C., Jones C., Mullaney J. R., Trichas M., 2012, ApJ, 755, 5

Guainazzi M., Bianchi S., 2007, MNRAS, 374, 1290

Harrison F. A. et al., 2013, ApJ, 770, 103

Hönig S. F., Leipski C., Antonucci R., Haas M., 2011, ApJ, 736, 26

Horst H., Gandhi P., Smette A., Duschl W. J., 2008, A&A, 479, 389

Ichikawa K., Ueda Y., Terashima Y., Oyabu S., Gandhi P., Matsuta K., Nakagawa T., 2012, ApJ, 754, 45

Ishihara D. et al., 2010, A&A, 514, A1

Itoh T. et al., 2008, PASJ, 60, 251

Iwasawa K., Fabian A. C., Matt G., 1997, MNRAS, 289, 443

Jarrett T. H. et al., 2011, ApJ, 735, 112

Kennicutt R. C., Jr, 1998, ARA&A, 36, 189

Kinkhabwala A. et al., 2002, ApJ, 575, 732

Kokubun M. et al., 2007, PASJ, 59, 53

Kondratko P. T., Greenhill L. J., Moran J. M., 2006, ApJ, 652, 136

Koss M., Mushotzky R., Veilleux S., Winter L., 2010, ApJ, 716, L125

Koss M., Mushotzky R., Veilleux S., Winter L. M., Baumgartner W., Tueller J., Gehrels N., Valencic L., 2011, ApJ, 739, 57

Koyama K. et al., 2007, PASJ, 59, 23

Krabbe A., Böker T., Maiolino R., 2001, ApJ, 557, 626

Lagage P. O. et al., 2004, The Messenger, 117, 12

Levenson N. A., Radomski J. T., Packham C., Mason R. E., Schaefer J. J., Telesco C. M., 2009, ApJ, 703, 390

Liu Y., Li X., 2015, MNRAS, 448, L53

Lutz D., Maiolino R., Spoon H. W. W., Moorwood A. F. M., 2004, A&A, 418, 465

Madejski G., Życki P., Done C., Valinia A., Blanco P., Rothschild R., Turek B., 2000, ApJ, 535, L87

Magdziarz P., Zdziarski A. A., 1995, MNRAS, 273, 837

Maiolino R., Risaliti G., Salvati M., 1999, A&A, 341, L35

Marinucci A., Risaliti G., Wang J., Nardini E., Elvis M., Fabbiano G., Bianchi S., Matt G., 2012, MNRAS, 423, L6

Márquez I. et al., 1999, A&AS, 140, 1

Márquez I. et al., 2004, A&A, 416, 475

Maselli A. et al., 2013, ApJS, 206, 17

Mateos S. et al., 2005, A&A, 433, 855

Mateos S. et al., 2012, MNRAS, 426, 3271

Mateos S., Alonso-Herrero A., Carrera F. J., Blain A., Severgnini P., Caccianiga A., Ruiz A., 2013, MNRAS, 434, 941

Matsuta K. et al., 2012, ApJ, 753, 104

Matt G., Fabian A. C., Guainazzi M., Iwasawa K., Bassani L., Malaguti G., 2000, MNRAS, 318, 173

Meléndez M., Kraemer S. B., Weaver K. A., Mushotzky R. F., 2011, ApJ, 738, 6

Merloni A. et al., 2012, eROSITA Science Book: Mapping the Structure of the Energetic Universe, preprint (arXiv:1209.3114)

Mineo S., Gilfanov M., Sunyaev R., 2012, MNRAS, 426, 1870

Moshir M. et al., 1990, in IRAS Faint Source Catalogue, version 2.0 (1990). IPAC, Caltech, California, p. 0

Murphy K. D., Yaqoob T., 2009, MNRAS, 397, 1549

Nair P. B., Abraham R. G., 2010, ApJ, 714, L260

Panessa F., Bassani L., Cappi M., Dadina M., Barcons X., Carrera F. J., Ho L. C., Iwasawa K., 2006, A&A, 455, 173

Piconcelli E., Jimenez-Bailón E., Guainazzi M., Schartel N., Rodríguez-Pascual P. M., Santos-Lleó M., 2005, A&A, 432, 15

Planck Collaboration XVI, 2014, A&A, 571, A16

Puccetti S. et al., 2014, ApJ, 793, 26

Ramos Almeida C. et al., 2011, ApJ, 731, 92

Ricci C., Ueda Y., Ichikawa K., Paltani S., Boissay R., Gandhi P., Stalevski M., Awaki H., 2014, A&A, 567, A142

Sako M., Kahn S. M., Paerels F., Liedahl D. A., 2000, ApJ, 543, L115

Sanders D. B., Mirabel I. F., 1996, ARA&A, 34, 749

Segreto A., Cusumano G., Ferrigno C., La Parola V., Mangano V., Mineo T., Romano P., 2010, A&A, 510, A47

Severgnini P., Caccianiga A., Della Ceca R., Braito V., Vignali C., La Parola V., Moretti A., 2011, A&A, 525, A38

Smith R. K., Brickhouse N. S., Liedahl D. A., Raymond J. C., 2001, ApJ, 556, L91

Stern D. et al., 2012, ApJ, 753, 30

Takahashi T. et al., 2007, PASJ, 59, 35

Takahashi T. et al., 2012, in Takahashi T., Murray S. S., den Herder J.-W. A., eds, Proc. SPIE Conf. Ser. Vol. 8443, Space Telescopes and Instrumentation 2012: Ultraviolet to Gamma Ray. SPIE, Bellingham, p. 84431Z

Theureau G., Hanski M. O., Coudreau N., Hallet N., Martin J.-M., 2007, A&A, 465, 71

Treister E., Urry C. M., Virani S., 2009, ApJ, 696, 110

Tueller J., Mushotzky R. F., Barthelmy S., Cannizzo J. K., Gehrels N., Markwardt C. B., Skinner G. K., Winter L. M., 2008, ApJ, 681, 113

Tueller J. et al., 2010, ApJS, 186, 378

Ueda Y. et al., 2007, ApJ, 664, L79

Ueda Y., Akiyama M., Hasinger G., Miyaji T., Watson M. G., 2014, ApJ, 786, 104

Vasudevan R. V., Brandt W. N., Mushotzky R. F., Winter L. M., Baumgartner W. H., Shimizu T. T., Schneider D. P., Nousek J., 2013, ApJ, 763, 111

Weaver K. A. et al., 2010, ApJ, 716, 1151

Winter L. M., Mushotzky R. F., Reynolds C. S., Tueller J., 2009, ApJ, 690, 1322

Wright E. L. et al., 2010, AJ, 140, 1868

Yaqoob T., 2012, MNRAS, 423, 3360

This paper has been typeset from a TEX/LATEX file prepared by the author.